

Superresolving masks for incoherent high-numerical-aperture scanning microscopy in three dimensions

Ibrahim Akduman,* Ulrich Brand, Jan Grochmalicki, Gerard Hester, and Roy Pike

Department of Physics, King's College London, Strand, London WC2R 2LS, UK

Mario Bertero

Istituto di Fisica, Università di Genova and Istituto Nazionale di Fisica Nucleare, Via Dodecaneso 33, I-16146 Genova, Italy

Received January 27, 1998; accepted May 4, 1998

A singular-value-decomposition analysis of the imaging kernel for three-dimensional fluorescent laser scanning microscopy at a high numerical aperture (NA) is presented. The design and superresolving performance of image-plane binary optical masks are then derived, and new computational techniques for calculating these masks are given. Initial experimental results with a microscope equipped with such a mask at $NA = 1.3$ are presented. The improvement in both contrast and resolution over the confocal and type 1 instruments is demonstrated. © 1998 Optical Society of America [S0740-3232(98)03809-5]

OCIS codes: 180.1790, 180.2520, 180.5810, 180.6900, 070.4560.

1. INTRODUCTION

In previous studies¹⁻⁴ we described the use of optical masks in scanning confocal microscopy to achieve resolution beyond that which can be obtained in conventional imaging systems. A mask of this kind is installed in place of the pinhole of the confocal arrangement, and its profile is designed to implement the data-inversion algorithm derived from singular-system theory. For practical reasons the continuous-mask profiles are approximated by arrays of concentric binary rings. Also, for incoherent light, to implement the positive and negative values of the theoretical mask function, the mask is inserted at 45° to the illuminating beam and two integrating detectors are used to collect both the transmitted and reflected signals, which are then subtracted.

In previous work with both coherent and incoherent light, the above program was realized for the two-dimensional case with low numerical apertures (NA's) and the theoretical predictions were confirmed experimentally. In this paper we present the full three-dimensional high-NA case.

In the low-NA cases, the simple theoretical expressions for paraxial imaging allowed the computations to be performed without great difficulty and provided an academic basis for proving the fundamental concepts of such systems and for testing them in practice. Owing to the seemingly impossible computational load, the goal of designing a high-aperture system that is based on the same principles for application in real-life microscopy has, however, seemed for a number of years to be somewhat far off.

A significant step toward this goal was taken by Bertero *et al.* in 1990⁵ when they carried out a preliminary calculation of the singular system of a high-aperture sys-

tem for $NA = 1.3$. In that paper, owing to the numerical difficulty of the problem, only a small number of sampling points was used and there was no feasible way to control the convergence, with the effect that the accuracy of the results remained somewhat uncertain. Then in 1994 a reliable computation of the singular system of a low-NA system for one radial and one axial coordinate was presented in Ref. 6.

In the present paper, expanding on the work of Ref. 5, we implement a new way to solve the full three-dimensional case through the use of a novel sampling tactic. In this way we are able to carry out what to our knowledge is the first complete singular-value-decomposition (SVD) analysis, giving both the spectrum and the singular functions, of the imaging of the high-NA fluorescence microscope. The new sampling method is based on a little-known analytic expression for an integral of a product of three Bessel functions. Use of this formula reduces the computational problem to manageable proportions, which allows for the control of numerical accuracy. With this method we are able to sample the imaging kernel and compute its SVD in less than 30 min on a Dec Alpha 600 workstation (Digital Equipment Corporation, Maynard, Mass.). With these results, a new optical mask was designed and built that performs the analog implementation of an SVD-based, data-inversion algorithm. Numerical simulations of the performance of a microscope that uses this mask have been carried out, and the resolution gains are assessed. These have been confirmed by preliminary experimental results.

The paper is organized as follows. In Section 2 we describe the high-aperture incoherent imaging problem in confocal scanning microscopy and recapitulate the theo-

retical principles of a superresolving solution by means of an optical mask. In Section 3 the problem is reduced to a matrix form by exact sampling theorems, and in Section 4 we show how the discretized kernel is computed. The singular system and the form of the mask are discussed in Section 5. In Section 6, on the basis of these principles, we analyze the performance characteristics of a practical microscope that uses an objective lens with $\text{NA} = 1.3$. The singular system we obtain is in good agreement with that of Ref. 5, and the calculated performance characteristics demonstrate convincingly the usefulness of optical masks of our design for achieving superresolution in the lateral and, for certain truncation values k , also in the axial direction. In Section 7 we present initial experimental results that demonstrate a performance close to our theoretical predictions, with a test specimen kindly provided by the Cornell Nanofabrication Facility (Ithaca, N.Y.).

2. SINGULAR-VALUE-DECOMPOSITION THEORY OF A SUPERRESOLVING OPTICAL MASK

Since in a confocal system the objective and collector lenses have a common focal point at the specimen, this point will be chosen as the origin of the coordinate system. The optical axis will be adopted as the z axis, such that $z = 0$ coincides with the confocal plane. Throughout, we shall use the mixed cylindrical-polar, three-dimensional, coordinate system $[\boldsymbol{\rho} = (\rho, \theta), z]$, with the dimensionless system of optical units⁷ defined by

$$\begin{aligned} x &= \frac{2n \sin \alpha}{\lambda} x_0, & y &= \frac{2n \sin \alpha}{\lambda} y_0, \\ z &= \frac{2n \sin^2 \alpha}{\lambda} z_0, \end{aligned} \quad (2.1)$$

where x_0, y_0, z_0 are the standard geometrical coordinates,

$$\text{NA} = n \sin \alpha \quad (2.2)$$

is the NA of the microscope objective lens, and λ is the wavelength of the excitation light. Here α denotes the semiangle of acceptance of the objective lens and n denotes the refractive index of the objective immersion oil. In this paper we will use the value $\text{NA} = 1.3$, which for the standard immersion oil of $n = 1.518$ gives $\alpha = 58.9^\circ$.

Without narrowing our scope too much, for practical purposes we assume that

1. The optical system is rotationally invariant around the optical axis.
2. The lenses and immersion system are aberration free.
3. The excitation light is circularly polarized.
4. The fluorescent material is weakly absorbing so that incident light is not appreciably depleted in passing through the specimen.
5. The fluorescent radiation is completely incoherent and randomly polarized.

6. The slight difference between the wavelength of the excitation radiation and the wavelength of the fluorescence is negligible.

Let us consider a three-dimensional fluorescent object and denote the distribution function of its fluorescent centers by $f(\boldsymbol{\rho}, z)$. Under the assumptions listed above, the basic imaging equation of the scanning confocal microscope (see, for example, Ref. 5) gives the intensity distribution in the image plane as

$$g(\boldsymbol{\rho}) = \int W_2(|\boldsymbol{\rho} - \boldsymbol{\rho}'|, z') W_1(|\boldsymbol{\rho}'|, z') f(\boldsymbol{\rho}', z') d\boldsymbol{\rho}' dz', \quad (2.3)$$

where $W_1(|\boldsymbol{\rho}|, z)$ and $W_2(|\boldsymbol{\rho}|, z)$ are the rotationally symmetric point-spread functions (PSF's) (i.e., the time-averaged energy distributions in the focal region) of the illuminating lens and the imaging lens, respectively. We shall consider here the confocal microscope working in the epifluorescence mode with a single lens for both illumination and imaging, so that

$$W_1(\rho, z) = W_2(\rho, z) \equiv W(\rho, z). \quad (2.4)$$

Concerning the illumination defined by the assumptions above and for lenses with high NA's, we use the full expression for the circularly symmetric PSF $W(\rho, z)$, derived first by Ignatowsky⁷ (see also, Richards and Wolf⁸) as

$$W(\rho, z) = |I_0(\rho, z)|^2 + 2|I_1(\rho, z)|^2 + |I_2(\rho, z)|^2, \quad (2.5)$$

where

$$\begin{aligned} I_0(\rho, z) &= \int_0^\alpha (\cos \theta)^{1/2} \sin \theta (1 + \cos \theta) \\ &\quad \times J_0\left(\frac{\sin \theta}{\sin \alpha} \rho\right) \exp\left(i \frac{\cos \theta}{\sin^2 \alpha} z\right) d\theta, \end{aligned} \quad (2.6)$$

$$\begin{aligned} I_1(\rho, z) &= \int_0^\alpha (\cos \theta)^{1/2} \sin^2 \theta J_1\left(\frac{\sin \theta}{\sin \alpha} \rho\right) \\ &\quad \times \exp\left(i \frac{\cos \theta}{\sin^2 \alpha} z\right) d\theta, \end{aligned} \quad (2.7)$$

$$\begin{aligned} I_2(\rho, z) &= \int_0^\alpha (\cos \theta)^{1/2} \sin \theta (1 - \cos \theta) J_2\left(\frac{\sin \theta}{\sin \alpha} \rho\right) \\ &\quad \times \exp\left(i \frac{\cos \theta}{\sin^2 \alpha} z\right) d\theta. \end{aligned} \quad (2.8)$$

Our problem is to find the function $f(\boldsymbol{\rho}', z')$ for a given g . In fact, since scanning is involved, it is sufficient to recover only $f(0, 0)$, i.e., the value of the object at the confocal point. Complete reconstruction of f can then be achieved by repeating this procedure at each scanning position.

To solve the Fredholm equation (2.3), we consider its singular system, say $\{\alpha_k; u_k, v_k\}$, $k = 0, 1, 2, \dots$, which is defined as the set of solutions of the coupled integral equations

$$\mathbf{A} u_k = \alpha_k v_k, \quad \mathbf{A}^* v_k = \alpha_k u_k, \quad (2.9)$$

where \mathbf{A} is defined by the integral operator of Eq. (2.3) and \mathbf{A}^* denotes its adjoint, given by

$$(\mathbf{A}^*g)(\boldsymbol{\rho}, z) = W(\boldsymbol{\rho}, z) \int W(|\boldsymbol{\rho} - \boldsymbol{\rho}'|, z)g(\boldsymbol{\rho}')d\boldsymbol{\rho}'. \quad (2.10)$$

In Eq. (2.9), α_k stands for the k th singular value of the system, while $u_k(\boldsymbol{\rho}, z)$ and $v_k(\boldsymbol{\rho})$ are the singular functions spanning the object and image domains, respectively. Notice that these functions provide complete orthonormal bases in the corresponding domains.

An approximate solution (truncated singular-value decomposition) of the inverse problem stated above is given by

$$f(0, 0) = \sum_{k=0}^{K-1} \frac{1}{\alpha_k} (g, v_k)u_k(0, 0). \quad (2.11)$$

The number of terms K in the summation is limited by the noise affecting the data (cf. Ref. 9). In Eq. (2.11), (g, v_k) is the scalar product of g and v_k ; namely,

$$(g, v_k) = \int g(\boldsymbol{\rho})v_k(\boldsymbol{\rho})d\boldsymbol{\rho}. \quad (2.12)$$

By substituting this expression into Eq. (2.11) and then changing the order of summation and integration, one gets

$$f(0, 0) = \int M(\boldsymbol{\rho}')g(\boldsymbol{\rho}')d\boldsymbol{\rho}', \quad (2.13)$$

where

$$M(\boldsymbol{\rho}) = \sum_{k=0}^{K-1} \frac{1}{\alpha_k} u_k(0, 0)v_k(\boldsymbol{\rho}). \quad (2.14)$$

As follows from Eq. (2.13), to solve the problem one first multiplies the image intensity g with a known function $M(\boldsymbol{\rho})$, which is determined by the singular system, and then spatially integrates the result. The function $M(\boldsymbol{\rho})$ will be called the optical mask. The multiplication and spatial integration are both analog operations that can be implemented optically, which allows the processing to be carried out prior to detection.

The most important property of $W(\boldsymbol{\rho}, z)$ is that its Fourier transform

$$\begin{aligned} \hat{W}(\boldsymbol{\omega}, \eta) &= \int_{\mathbf{R}^3} W(\boldsymbol{\rho}, z)\exp(-i(\boldsymbol{\rho}, \boldsymbol{\omega}) - i\eta z)d\boldsymbol{\rho}dz \\ &= 2\pi \int_0^{+\infty} \rho d\rho \int_{-\infty}^{+\infty} dz J_0(\omega\rho)\exp(-i\eta z)W(\rho, z), \end{aligned} \quad (2.15)$$

where $\boldsymbol{\omega} = (\omega_1, \omega_2)$, is bounded, with support contained within a cylinder

$$|\boldsymbol{\omega}| \leq \Omega_{\perp}, \quad |\eta| \leq \Omega_{\parallel}, \quad (2.16)$$

where

$$\Omega_{\perp} = 2\pi, \quad \Omega_{\parallel} = \frac{\pi}{1 + \cos \alpha}. \quad (2.17)$$

It can be noted here that, in view of the above, the use of higher-NA lenses implies the enhancement of the ratio between axial and lateral resolution. It can also be shown that

1. $\hat{g}(\boldsymbol{\omega})$ has its support in the circle $|\boldsymbol{\omega}| \leq \Omega_{\perp}$.
2. $\hat{f}(\boldsymbol{\omega}, \eta)$ has its support in the cylinder $|\boldsymbol{\omega}| \leq 2\Omega_{\perp}$, $|\eta| \leq 2\Omega_{\parallel}$.

With these properties it can be demonstrated that the integral operator (2.3) is of the Hilbert–Schmidt class and is therefore compact. The line of the proof follows that of Ref. 6.

In Section 3 we shall analyze the circularly symmetric case and then discretize the resulting integral equation, using sampling theorems to find the singular system.

3. THEORY OF SAMPLING OF THE IMAGING KERNEL

The singular system for this case can be determined only numerically. This is done by means of the discretization of the operator \mathbf{A} by use of sampling theory.¹⁰ Using these components one can calculate the mask function. Since the optical system is circularly symmetric and since we are interested in recovering the object only at the axial point, the solution of this problem is invariant with respect to rotations about the optical axis. This observation is justified by point 3 above and by the long lifetime of the fluorescent emission compared with an optical cycle. This implies that we can simplify our inverse problem by replacing both the full image g and the full object f with their axially averaged projections

$$\begin{aligned} g_0(\rho) &= \frac{1}{2\pi} \int_0^{2\pi} g(\rho, \phi)d\phi, \\ f_0(\rho', z') &= \frac{1}{2\pi} \int_0^{2\pi} f(\rho', \phi'; z')d\phi' \end{aligned} \quad (3.1)$$

on the subspace of functions with circular symmetry. In the above, (ρ, ϕ) and (ρ', ϕ') denote the polar coordinates describing $\boldsymbol{\rho}$ and $\boldsymbol{\rho}'$, respectively. As the singular functions u_k and v_k are now circularly symmetric, so is the resulting optical mask [cf. Eq. (2.14)]. Consequently, it must be noted that only the rotationally invariant component of the image function g contributes now to the scalar product (2.13); the angular integration on the right-hand side of Eq. (2.13) can be carried out, and as a result g_0 replaces g . As the identity $f(0, 0) \equiv f_0(0, 0)$ is obvious, we can limit ourselves to the radial inverse problem, and thus Eq. (2.3) can now be rewritten as

$$\begin{aligned} g_0(\rho) &= (\mathbf{A}_0 f_0)(\rho) \\ &= \int_0^{\infty} \int_{-\infty}^{+\infty} W_0(\rho, \rho'; z')W(\rho', z') \\ &\quad \times f_0(\rho', z')\rho'd\rho'dz', \end{aligned} \quad (3.2)$$

where

$$W_0(\rho, \rho'; z') = \int_0^{2\pi} W[(\rho^2 + \rho'^2 - 2\rho\rho' \cos \beta)^{1/2}, z'] d\beta. \quad (3.3)$$

Evidently, $g_0(\rho)$ is the mean value of $g(\rho, \phi)$ over the circle of radius ρ , and $f_0(\rho', z')$ has a similar meaning. Also, because of Eq. (2.16), it can be demonstrated that

1. The Hankel transform of $g_0(\rho)$ has support in $\omega \leq \Omega_\perp$.
2. The Hankel transform of $f_0(\rho', z')$ with z' fixed has support in $0 \leq \omega \leq 2\Omega_\perp$, while its Fourier transform with respect to z' with ρ' fixed has support in $|\eta| \leq 2\Omega_\parallel$.

In the above, by a Hankel transform of a function h , we understand that

$$\tilde{h}(\omega) = \int_0^\infty \rho J_0(\omega\rho) h(\rho) d\rho, \quad (3.4)$$

where J_0 is the zero-order Bessel function of the first kind. Defined in this way, for rotationally symmetric functions this transform is equivalent to the ordinary Fourier transform.

In terms of the projected functions, the new singular system of the problem, say, $\{\alpha_{0,k}; u_{0,k}, v_{0,k}\}$, will be the solutions of the coupled homogeneous equations

$$\mathbf{A}_0 u_{0,k} = \alpha_{0,k} v_{0,k}, \quad \mathbf{A}_0^* v_{0,k} = \alpha_{0,k} u_{0,k}, \quad (3.5)$$

where \mathbf{A}_0^* is the adjoint of \mathbf{A}_0 given by

$$(\mathbf{A}_0^* g_0)(\rho) = W(\rho, z) \int_0^\infty W_0(\rho, \rho'; z) g_0(\rho') \rho' d\rho'. \quad (3.6)$$

To tackle this system, below we will develop a practical method of discretizing this problem.

If the function h is Hankel band limited, with bandwidth Ω , it can be expressed by means of the so-called sampling expansion¹⁰ as

$$h(\rho) = \sum_{n=1}^\infty \frac{2x_n}{J_1(x_n)} h(x_n/\Omega) \frac{J_0(\Omega\rho)}{x_n^2 - (\Omega\rho)^2}. \quad (3.7)$$

In other words, $h(\rho)$ can be expressed in terms of its values at the sampling points $\rho_n = x_n/\Omega$, x_n being the n th zero of $J_0(x)$. If we introduce the functions

$$S_n(\Omega, \rho) = \Omega \sqrt{2} \frac{x_n J_0(\Omega\rho)}{x_n^2 - (\Omega\rho)^2}, \quad n = 1, 2, \dots \quad (3.8)$$

Equation (3.7) can be rephrased as

$$h(\rho) = \sum_{n=1}^\infty \frac{\sqrt{2}}{\Omega J_1(x_n)} h(x_n/\Omega) S_n(\Omega, \rho). \quad (3.9)$$

In fact, it can be demonstrated that in the space of circularly symmetric and band-limited functions the functions $S_n(\Omega, \rho)$ form an orthonormal basis, i.e.,

$$\int_0^\infty S_n(\Omega, \rho) S_m(\Omega, \rho) \rho d\rho = \delta_{nm}, \quad (3.10)$$

and also

$$\int_0^\infty \rho S_n(\Omega, \rho) h(\rho) d\rho = \frac{\sqrt{2}}{\Omega J_1(x_n)} h(x_n/\Omega). \quad (3.11)$$

Since the Hankel transforms of the projected functions $f_0(\rho', z')$ and $g_0(\rho)$ have bandwidths $2\Omega_\perp$ and Ω_\perp , respectively, in their case the sampling expansion yields

$$f_0(\rho', z') = \sum_{m=1}^\infty \frac{\sqrt{2}}{2\Omega_\perp J_1(x_m)} \times f_0(x_m/2\Omega_\perp, z') S_m(2\Omega_\perp, \rho'), \quad (3.12)$$

and by substituting Eq. (3.12) into Eq. (3.2) and then using the resulting equation for the sampled values of $g_0(\rho)$ at the points $\rho_n = x_n/\Omega_\perp$ and by invoking the property (3.11),

$$g_0\left(\frac{x_n}{\Omega_\perp}\right) = \sum_{m=1}^\infty \frac{2}{(2\Omega_\perp)^2 J_1^2(x_m)} \int_{-\infty}^{+\infty} W_0\left(\frac{x_n}{\Omega_\perp}, \frac{x_m}{2\Omega_\perp}; z'\right) \times W\left(\frac{x_m}{2\Omega_\perp}, z'\right) f_0\left(\frac{x_m}{2\Omega_\perp}, z'\right) dz'. \quad (3.13)$$

On the other hand, since functions $f_0(x_m/2\Omega_\perp, z')$, as functions of the variable z' , are band limited with bandwidth $2\Omega_\parallel$, from the usual one-dimensional Whittaker-Shannon sampling theorem, we obtain

$$f_0\left(\frac{x_m}{2\Omega_\perp}, z'\right) = \sum_{l=-\infty}^{+\infty} f_0\left(\frac{x_m}{2\Omega_\perp}, z_l\right) \times \text{sinc}\left[\frac{2\Omega_\parallel}{\pi}(z' - z_l)\right], \quad m = 1, 2, \dots, \quad (3.14)$$

where we have introduced

$$z_l = \frac{\pi}{2\Omega_\parallel} l, \quad l = 0, \pm 1, \pm 2, \dots \quad (3.15)$$

and

$$\text{sinc}\left[\frac{2\Omega_\parallel}{\pi}(z' - z_l)\right] = \frac{\pi \sin[2\Omega_\parallel(z' - z_l)]}{2\Omega_\parallel \pi(z' - z_l)}. \quad (3.16)$$

Since the product $W_0 W$ appearing in Eq. (3.13) is itself band limited with bandwidth $2\Omega_\parallel$, one also has

$$\int_{-\infty}^{+\infty} W_0\left(\frac{x_n}{\Omega_\perp}, \frac{x_m}{2\Omega_\perp}; z'\right) W\left(\frac{x_m}{2\Omega_\perp}, z'\right) \times \text{sinc}\left[\frac{2\Omega_\parallel}{\pi}(z' - z_l)\right] dz' = \frac{\pi}{2\Omega_\parallel} W_0\left(\frac{x_n}{\Omega_\perp}, \frac{x_m}{2\Omega_\perp}; z_l\right) W\left(\frac{x_m}{2\Omega_\perp}, z_l\right). \quad (3.17)$$

Finally, substitution of Eq. (3.14) into Eq. (3.13) with the help of Eq. (3.17) results in the linear system

$$b_n = \sum_{m=1}^\infty \sum_{l=-\infty}^{+\infty} \mathbf{A}_{n,m,l} a_{m,l}, \quad n = 1, 2, \dots, \quad (3.18)$$

where

$$\begin{aligned}
 b_n &= \frac{\sqrt{2}}{\Omega_\perp J_1(x_n)} g_0\left(\frac{x_n}{\Omega_\perp}\right), \\
 a_{m,l} &= \left(\frac{\pi}{2\Omega_\parallel}\right)^{1/2} \frac{\sqrt{2}}{2\Omega_\perp J_1(x_m)} f_0\left(\frac{x_m}{2\Omega_\perp}, z_l\right), \\
 \mathbf{A}_{n,m,l} &= \left(\frac{\pi}{2\Omega_\parallel}\right)^{1/2} \frac{W_0\left(\frac{x_n}{\Omega_\perp}, \frac{x_m}{2\Omega_\perp}; z_l\right) W\left(\frac{x_m}{2\Omega_\perp}, z_l\right)}{\Omega_\perp^2 J_1(x_n) J_1(x_m)}.
 \end{aligned} \tag{3.19}$$

$$\tag{3.20}$$

The singular values of the infinite-dimensional matrix (3.20) coincide with the singular values of the integral operator (3.2). Approximations of these singular values can be computed by considering finite sections of the matrix (3.20) that are obtained by limiting the values of the indices to

$$\begin{aligned}
 n &= 1, 2, \dots, N_0, & m &= 1, 2, \dots, M_0, \\
 l &= 0, \pm 1, \pm 2, \dots, \pm L_0.
 \end{aligned} \tag{3.21}$$

As $N_0, M_0, L_0 \rightarrow \infty$, the singular values of the finite-dimensional matrix will converge to the singular values of the continuous operator. If we denote now by $U_{m,l}^{(k)}$ and $V_n^{(k)}$ the components of the singular vectors of the finite dimensional matrix (normalized to unity with respect to Euclidean norm), then from Eqs. (3.19) together with similarly truncated sampling expansions the approximations to the singular functions of the integral operator (3.2) can be expressed as

$$\begin{aligned}
 v_k(\rho) &= 2\pi\sqrt{2} \sum_{n=1}^{N_0} V_n^{(k)} \frac{x_n J_0(2\pi\rho)}{x_n^2 - (2\pi\rho)^2}, \\
 u_k(\rho, z) &= 4 \left(\frac{2\pi}{1 + \cos \alpha}\right)^{1/2} \sum_{m=1}^{M_0} \sum_{l=-L_0}^{L_0} \\
 &\quad \times U_{m,l}^{(k)} \frac{x_m J_0(4\pi\rho)}{x_m^2 - (4\pi\rho)^2} \operatorname{sinc}\left[\frac{2(z' - z_l)}{1 + \cos \alpha}\right].
 \end{aligned} \tag{3.22}$$

$$\tag{3.23}$$

Using these formulas in Eq. (2.14), we obtain the super-resolving mask.

4. COMPUTATION OF THE DISCRETIZED KERNEL

Calculation of the kernel matrix of Eq. (3.20) requires computation of the function $W(\rho, z)$ and its projection $W_0(\rho, \rho'; z)$ onto the subspace of circularly symmetric functions [cf. Eq. (3.3)]. Owing to the complicated nature of the PSF in the high-NA case [expressions (2.6)–(2.8)], calculation of the integral appearing in Eq. (3.3) is the most difficult part of the whole computation. The straightforward method, in which one numerically evaluates the double integral, is painstakingly slow, and its accuracy is rather difficult to control.

To find a more suitable method, let us return to the function W . Since its Hankel transform has the bandwidth $\Omega_\perp = 2\pi$, then according to the sampling expansion (3.9) we can write

$$W(\rho, z) = \sum_{k=1}^{\infty} W_k(z) S_k(2\pi, \rho), \tag{4.1}$$

where

$$W_k(z) = \frac{\sqrt{2}}{2\pi J_1(x_k)} W\left(\frac{x_k}{2\pi}, z\right). \tag{4.2}$$

In the following we will also need to remember the identity¹¹

$$\begin{aligned}
 \int_0^{2\pi} S_k[2\pi, (\rho^2 + \rho'^2 - 2\rho\rho' \cos \theta)^{1/2}] d\theta \\
 = \frac{1}{\rho'} S_k(2\pi, \rho) * \delta(\rho - \rho'),
 \end{aligned} \tag{4.3}$$

where (*) denotes convolution and $\delta(\rho)$ is the Dirac delta distribution. This convolution can be evaluated with Hankel transform techniques to obtain

$$S_k(2\pi, \rho) * \delta(\rho - \rho') = \sqrt{2} \frac{4\pi^2 \rho'}{x_k J_1(x_k)} I\left(\rho, \rho', \frac{x_k}{2\pi}\right), \tag{4.4}$$

where we have introduced the symbol

$$I(a, b, c) = \int_0^{2\pi} J_0(ax) J_0(bx) J_0(cx) x dx. \tag{4.5}$$

Then, substituting Eq. (4.1) into Eq. (3.3) and by taking into account Eqs. (4.3) and (4.4), we obtain

$$W_0(\rho, \rho'; z) = 4\pi \sum_{k=1}^{\infty} \frac{W\left(\frac{x_k}{2\pi}, z\right)}{[J_1(x_k)]^2} I\left(\rho, \rho', \frac{x_k}{2\pi}\right). \tag{4.6}$$

To obtain $\mathbf{A}_{n,m,l}$ we have to take $\rho = x_n/2\pi$ and $\rho' = x_m/4\pi$ and calculate the sequence of integrals (4.5) for these values; namely,

$$I\left(\frac{x_n}{2\pi}, \frac{x_m}{4\pi}, \frac{x_k}{2\pi}\right), \quad k = 1, 2, \dots \tag{4.7}$$

Fortunately, integrals of this kind were already considered by Fettis in 1957.¹² The expressions below are derived directly from his formulas. If we denote

$$q \equiv \frac{x_n^2 + x_m^2/4 - x_k^2}{x_n x_m}, \tag{4.8}$$

then depending on whether $|q|$ is greater, equal to, or smaller than 1, the result assumes the following forms:

A. In the case $|q| > 1$ we have $|q| = \cosh \theta$, and for $q > 0$

$$\begin{aligned}
 I\left(\frac{x_n}{2\pi}, \frac{x_m}{4\pi}, \frac{x_k}{2\pi}\right) &= 8\pi^2 \frac{x_k J_1(x_k)}{x_n x_m} \\
 &\quad \times \sum_{p=1}^{\infty} J_p(x_n) J_p(x_m/2) \frac{\exp(-p\theta)}{\sinh(\theta)}.
 \end{aligned} \tag{4.9}$$

For $q < 0$ an alternating sign factor $(-1)^{p+1}$ has to be included in the sum.

B. In the case $|q| < 1$ we have $q = \cos \theta$, and

$$I\left(\frac{x_n}{2\pi}, \frac{x_m}{4\pi}, \frac{x_k}{2\pi}\right) = 8\pi^2 \frac{x_k J_1(x_k)}{x_n x_m} \times \sum_{p=1}^{\infty} J_p(x_n) J_p(x_m/2) \frac{\sin(p\theta)}{\sin(\theta)}. \quad (4.10)$$

C. The case $|q| = 1$ is a natural limit of the previous one. We have $q = \cos \theta$, where either $\theta = 0$ or $\theta = \pi$. In the two cases in Eq. (4.10) we have to replace $\sin(p\theta)/\sin(\theta)$ with its limiting value as $\theta \rightarrow 0$ or $\theta \rightarrow \pi$, respectively. In the first case it is p , while in the second it is $p(-1)^{p+1}$.

Crucial for this calculation of the discretized operator matrix $\mathbf{A}_{n,m,l}$ is the fact that we can use precalculated tables of $J_p(x_n)$ and $J_p(x_m/2)$ as well as the array of $W[x_k/(2\pi), z_l]/[J_1(x_k)]^2$. For each pair (n, m) , a series of coefficients (4.7) is calculated, which is then used unchanged for all values of l . Convergence of the final series is dynamically controlled, further reducing unnecessary computation. The simplicity of the resulting algorithm makes it very easy to implement and also susceptible to compiler optimization. In Section 5 we will present the numerical results for the singular system of the microscope together with the form of the resulting optical mask.

5. SINGULAR SYSTEM AND FORM OF THE MASK

The singular system for the kernel matrix whose elements were calculated by the technique given in Section 4 have been computed for various values of the parameters N_0 , M_0 , and L_0 , with a NAG library (Numerical Algorithm Group, Ltd., Oxford, UK) SVD routine. By increasing these parameters, we have observed that the convergence of the singular values is rather slow. However, for $N_0 = 70$, $M_0 = 140$, and $L_0 = 70$, we have found that increasing them further changes the resulting singular values only slightly (beyond the fourth significant digit), thus implying that a satisfactory degree of convergence has been achieved. In Table 1 we give results for the first nine singular values of this system. If we assume that the signal-to-noise ratio in our system does not

Table 1. First Nine Singular Values of the NA = 1.3 Fluorescence Microscope System

K	α_K/α_0 (%)
0	100
1	21.8
2	9.88
3	4.48
4	2.35
5	1.42
6	0.85
7	0.50
8	0.33

exceed 100, then only the first seven singular values will be significant owing to the regularizing cutoff [cf. (2.11)].

Figures 1 and 2 display the first eight transverse singular functions corresponding to the singular values given in Table 1.

Knowledge of these singular-system components allows for the evaluation of the mask function of Eq. (2.14). Figure 3 shows the form of the mask calculated for seven singular values (i.e., $K = 6$). It has a continuous profile and changes sign. These features make it rather difficult to implement the mask for the case of incoherent light, because it is not possible to have a negative light intensity. However, if two detectors are used (with separate light processing) and the final readout is formed by subtraction of their signals, one can easily obtain the correct result. The practical difficulty, however, of how to implement the continuous profile accurately remains.

A feasible solution to this problem is to use regions of wholly reflecting and wholly transmitting coatings on a glass plate inserted at 45° to the optical axis in the image plane (see Refs. 4 and 13). The light that passes through the uncoated parts of such a mask (and is measured by one detector) corresponds to the positive components of the mask profile, while the light that is reflected at 90° (and measured by a separate detector) corresponds to the negative components. The mirror design consists of prolate elliptical annuli (forming circles when orthoprojected onto the image plane). Their positions and widths are chosen to emulate as closely as possible the action of the computed mask.

A precise algorithm is described in Ref. 13. It approximates the radial weight of the continuous mask profile by a binary-valued function (with two values $+1$ and -1), which is, in a sense, close to the original while also retaining its zero crossings. Although our choice of a measure of closeness is quite arbitrary, its justification is the satisfactory performance of the resulting mask. A binary mask, constructed according to this description, is shown in Fig. 4.

6. PERFORMANCE ANALYSIS OF THE MICROSCOPE

To evaluate the performance characteristics of the microscope with the binary mask given in Section 5, we have to calculate its impulse response (PSF) together with its transfer function. We will compare the results with those of the type 1 microscope,¹⁴ the confocal scanning microscope, and also with a theoretical microscope, using the continuous mask of Fig. 3. The theoretical performance on a line test specimen (Ronchi grating) has also been calculated and will be used in the Section 7 for comparison with experimental results. The PSF and transfer function of the microscope with a mask can be obtained by rewriting the inversion formula (2.11) as

$$f(0, 0) = \int T(x, z) f(x, z) dx dz, \quad (6.1)$$

where

$$T(x, z) = W(x, z) \int W(|x - x'|) M(x') dx'. \quad (6.2)$$

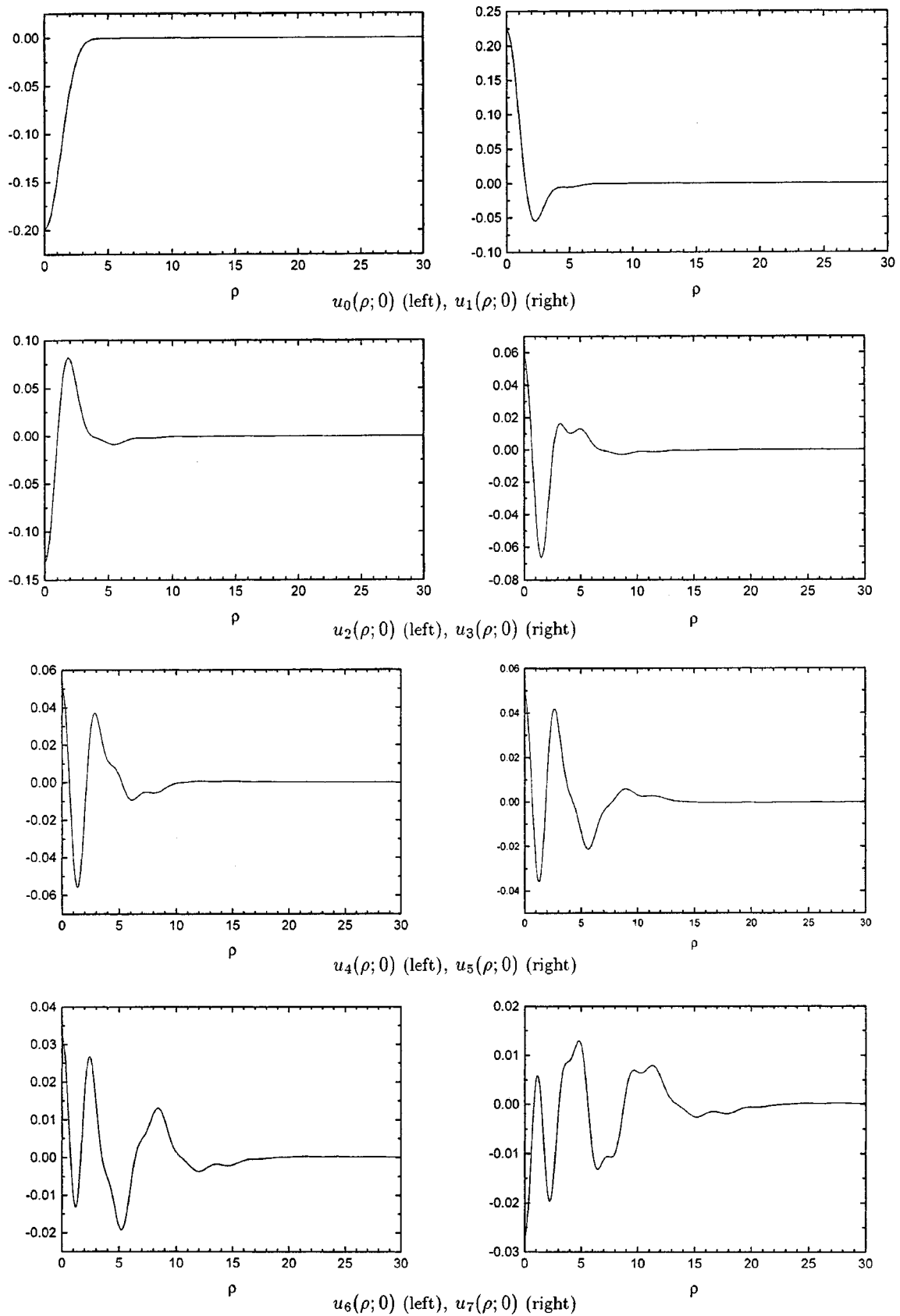


Fig. 1. First eight transverse singular functions $u_k(\rho, 0)$ in the $z = 0$ object plane corresponding to the singular values given in Table 1.

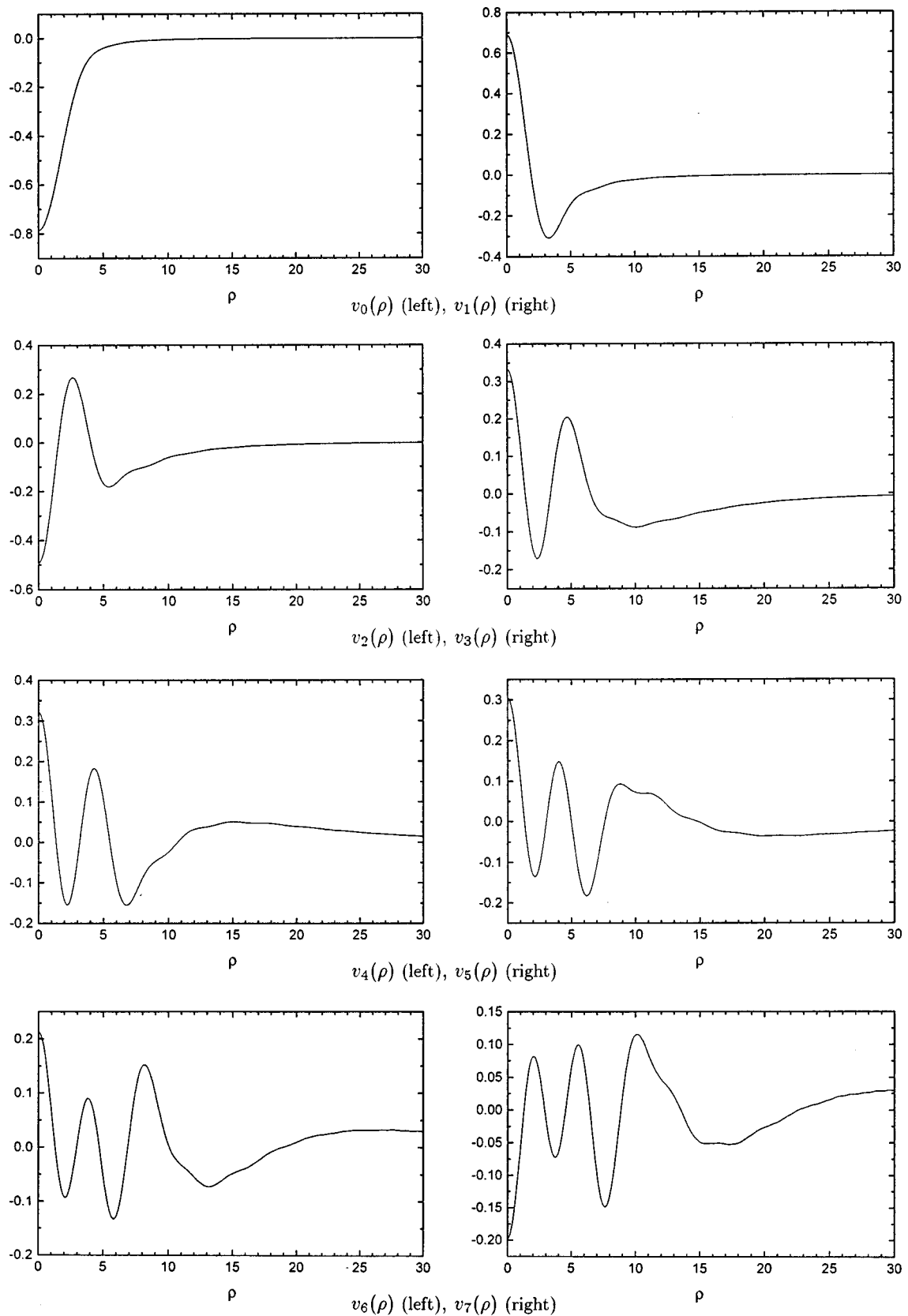


Fig. 2. First eight transverse singular functions $v_k(\rho)$ in the image plane corresponding to the singular values given in Table 1.

Equation (6.1) is derived from the fact that

$$f(0, 0) = (M, g) = (M, \mathbf{A}f) = (\mathbf{A}^*M, f). \quad (6.3)$$

Here $T(x, z)$ represents the impulse response of the microscope and can be calculated once the functions W and M are known. For the circularly symmetric case, the Hankel transform of $T(\rho, z)$ for a fixed z , $\hat{T}(\omega, z)$, gives the lateral frequency response or transfer function, while for a fixed ρ its Fourier transform with respect to z is the axial transfer function.

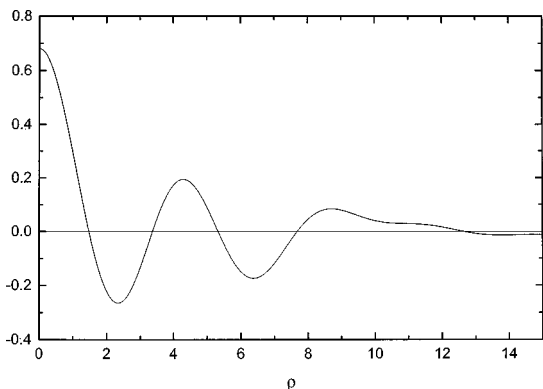
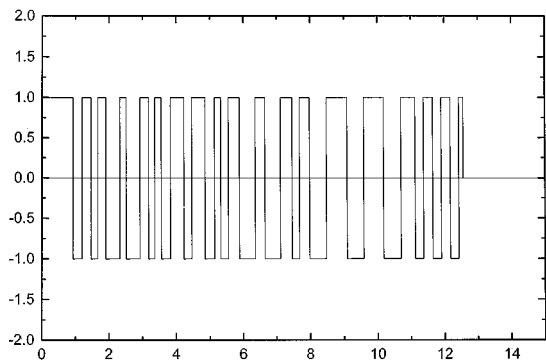
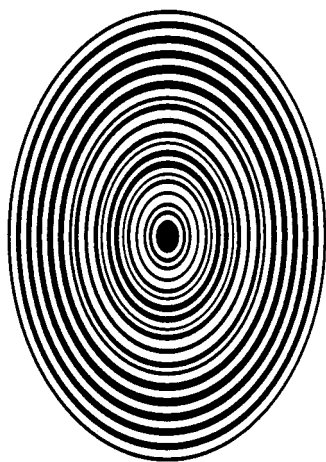


Fig. 3. Continuous-mask function for the superresolving microscope calculated with the singular functions of Figs. 1 and 2.



(a)



(b)

Fig. 4. (a) Approximate binary form of the superresolving mask of Fig. 3. (b) Design of the binary image-plane mask to be placed at 45° to the optical axis at the focal point.

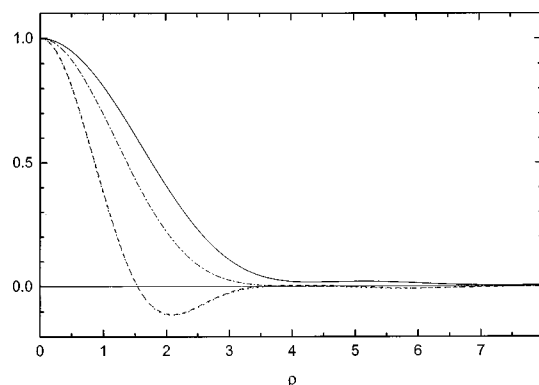


Fig. 5. Comparison of transverse sections of the PSF's at $z = 0$ between the superresolving designs, i.e., continuous (short-dashed curve) and binary (long-dashed curve) mask (indistinguishable on this scale) and the ordinary confocal (pinhole radius $\pi/2$) (dotted-dashed curve) and type 1 microscopes (solid curve). An increase of resolution of 57% at HWHM is achieved.

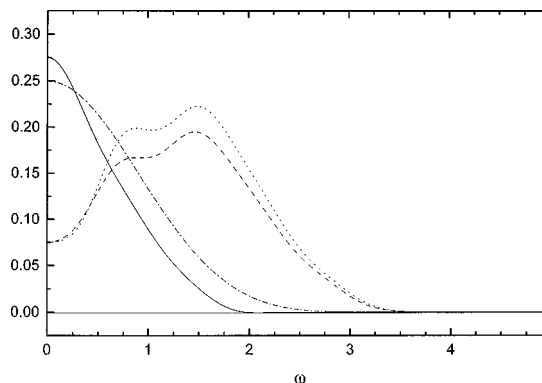


Fig. 6. Comparison of lateral transfer functions corresponding to the PSF's of Fig. 5. Improvement in the high-frequency response demonstrates the superresolving performance of the mask design. Type 1 microscope (solid curve), confocal microscope (dotted-dashed curve) and continuous (short-dashed curve) and binary mask (long-dashed curve) microscope.

Computational evaluation of the impulse response and the transfer function were performed by use of the convolution properties of Eq. (6.2). The Hankel transform was calculated with the quasi-fast Hankel transform technique of Siegman.¹⁵ With exponential sampling this method requires only two standard one-dimensional fast Fourier transform evaluations in order to obtain the Hankel transform with sufficient (and easily monitored) accuracy. As such, it is perfectly suited for numerical simulation.

In Fig. 5 the PSF's $T(\rho, 0)$ (corresponding to the continuous mask) and $T_b(\rho, 0)$ (corresponding to the binary mask) are compared with the PSF's of the type 1 and confocal scanning microscopes for $z = 0$. In other words, we compare their lateral resolutions at the focal point. It can be seen that the two mask-microscopes' PSF's are considerably sharper than those of the type 1 or confocal design and can be described as superresolving. If we consider the width of the central peak at its half-maximum as a measure of resolution, the continuous mask achieves a 57% increase in lateral resolution over that of a conventional confocal scanning microscope. The binary mask design yields an almost indistinguishable result.

The corresponding volume-normalized lateral transfer functions are displayed in Fig. 6. The improvement in lateral resolution can be seen in the behavior of $\hat{T}(\omega, 0)$ and $\hat{T}_b(\omega, 0)$ in the high-frequency region of the spectrum. The frequency response of the superresolving microscope is considerably stronger in this region.

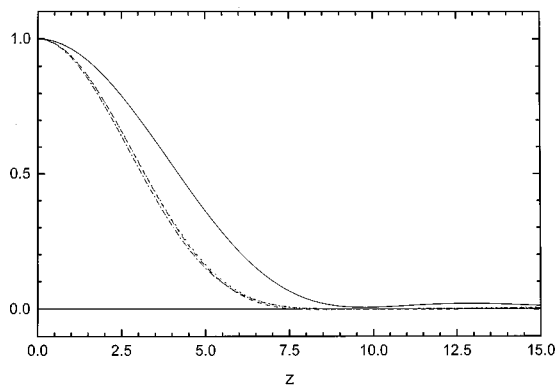


Fig. 7. Comparison of axial sections of the PSF's at $\rho = 0$ between the superresolving designs, i.e., the continuous (short-dashed curve) and binary (long-dashed curve) mask and the confocal (pinhole size $\pi/2$) (dotted-dashed curve) and type 1 (solid curve) microscopes. While the functions for the continuous and binary masks are virtually identical, both maintain the good axial performance of the confocal microscope (see Fig. 8).

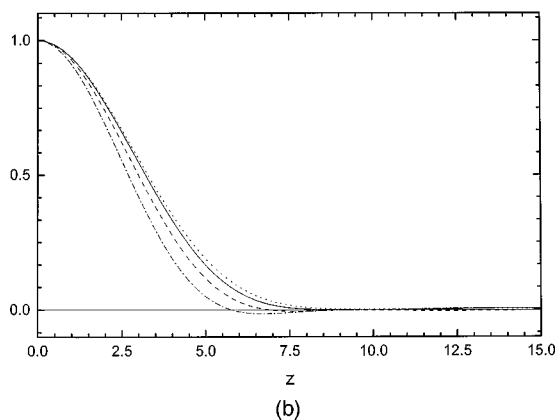
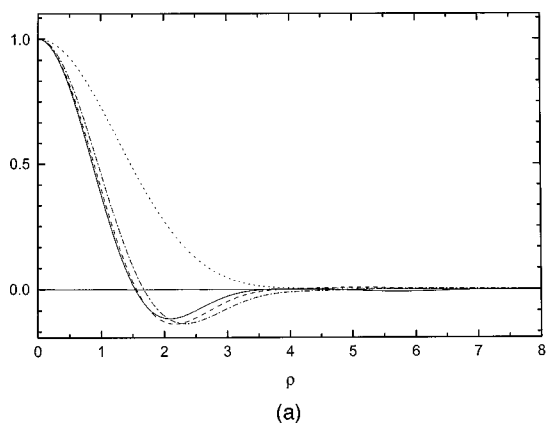


Fig. 8. (a) Transverse sections of the PSF at $z = 0$ and (b) axial sections at $\rho = 0$ for values of truncation number K from 0 to 6. A comparison with Fig. 7 reveals axial superresolution for $K = 2$ and $K = 4$, where $K = 0$ (short-dashed curve), $K = 2$ (dotted-dashed curve), $K = 4$ (long-dashed curve), and $K = 6$ (solid curve).

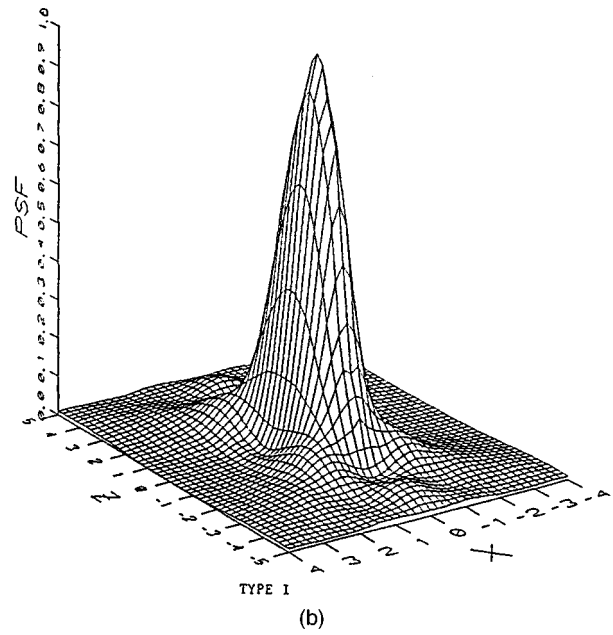
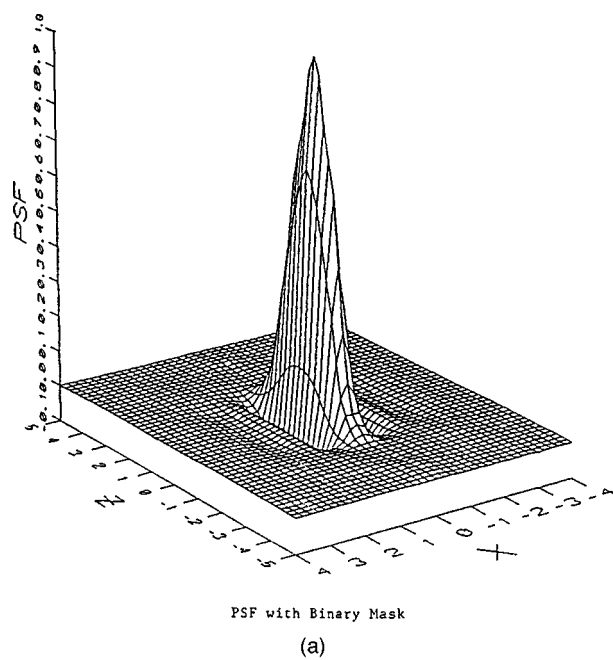


Fig. 9. x - z diagrams at $y = 0$ of the PSF's of (a) a $K = 6$ binary-mask superresolving microscope and (b) a type 1 microscope. $NA = 1.3$.

Figure 7 shows the axial PSF's at $\rho = 0$. As can be seen, both the continuous- and the binary-mask microscopes maintain the axial resolution of the confocal fluorescence microscope if seven singular functions are used ($K = 6$). A small improvement over the axial resolution of the confocal microscope is made possible by employing fewer functions. This is shown in Fig. 8(b), where the axial sections of the PSF for binary-mask microscopes with truncation values of $K = 0, 2, 4$, and 6 , i.e., with one, three, five, and seven singular functions, respectively, are presented. Apart from the case $K = 0$, the half-width of the central lobe in the axial direction is smaller than the half-width of the mask with $K = 6$ and thus is also smaller than that of the confocal microscope.

In Figs. 9(a) and 9(b) we show $x-z$ diagrams at $y = 0$ of the PSF's of a superresolving microscope with a $K = 6$ binary mask, and of a type 1 microscope, respectively. A twofold increase in transverse resolution and a 30% increase in axial resolution is achieved.

7. EXPERIMENTAL CONFIRMATION

An incoherent-imaging, superresolving, high-aperture, laser-scanning microscope has been built on the basis of above theoretical analysis of incoherent imaging. The microscope is modeled on the optical dimensions of the well-known Bio-Rad MRC1024 instrument (Bio-Rad Ltd., Hemstead, UK). A binary mask in the final image plane, calculated with the above results, performs the singular-value decomposition of the image intensity and superresolves images by instantaneous analogue optical processing.

The experimental setup is shown in Fig. 10. The laser is focused in the object plane by a set of lenses, the eyepiece (EP1), the tube lens (TL1), and the objective lens (OL). At $\lambda = 488$ nm and NA=1.3, the radius of the central lobe of the Airy pattern amounts to just under 230 nm. The experiments were performed with a test pattern supplied by the Cornell Nanofabrication Facility, consisting of a periodic set of bars and spacings, each 125-nm wide (resulting in a 250-nm period). The objective lens gathers the fluorescent light from fluorescein isothiocyanate stained polystyrene beads covering the rear surface of the test pattern, at the central wavelength

$\lambda_c = 520$ nm. A narrow-bandpass filter with a window of 25 nm around λ_c is fitted to eliminate any undesirable stray light in the system.

Along the detection path we create real images at two points before the final image plane, where the overall magnification is set to $m = 3300$ as in the Bio-Rad instrument. The use of such large magnification also allows a simple photoetching technique to be used for fabrication of the mask.

At the image plane the mask splits the image beam into two parts; the reflected light is measured by one detector, PMT_R , while the complementary transmitted part is registered by PMT_T . The difference of the signals from the two detectors yields the superresolved pixel value, while the sum gives the signal value of the ordinary type 1 microscope at the same instant. A confocal image can also be produced by reducing the size of the diaphragm in front of the reflection-arm detector, although it cannot be obtained simultaneously in our present system.

The mask design is shown in Fig. 4 and was described in Section 5. Because of its insertion at 45° , its pattern consists of concentric fully reflective and transmissive elliptic rings. The maximum dimensions correspond to a projected circular diameter of 5.0 mm.

After careful alignment, the instrument is calibrated for the relative sensitivity of the two detectors. A zero level is chosen in order to suppress the impact of auto-fluorescence produced by the immersion oil and the mounting fluid as well as of constant stray light.

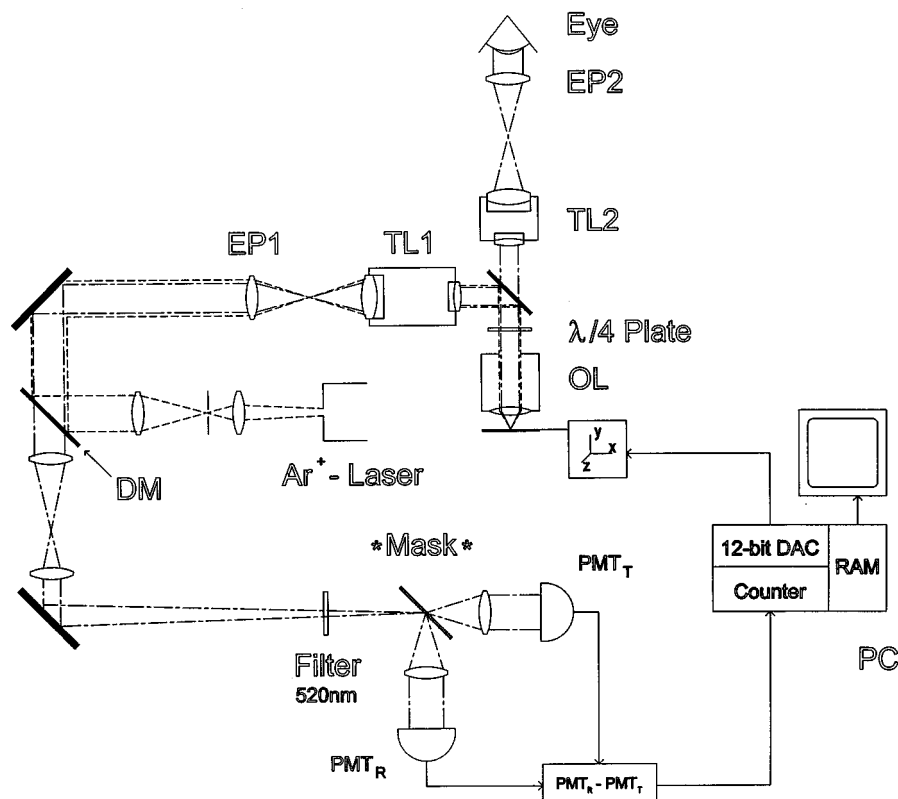


Fig. 10. Schematic diagram of the experimental microscope. EP, eyepiece; DM, dichroic mirror; TL, tube lens; OL, objective lens.

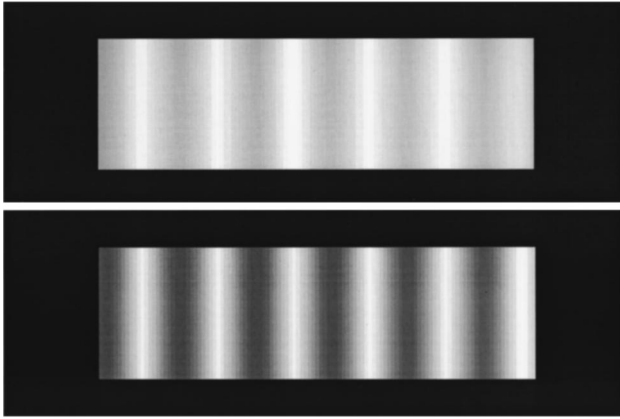


Fig. 11. Calculated image of a set of parallel bars. Bars are 125 nm wide, separated by another 125 nm. The upper image corresponds to a type 1 microscope, and the lower to our superresolving microscope.

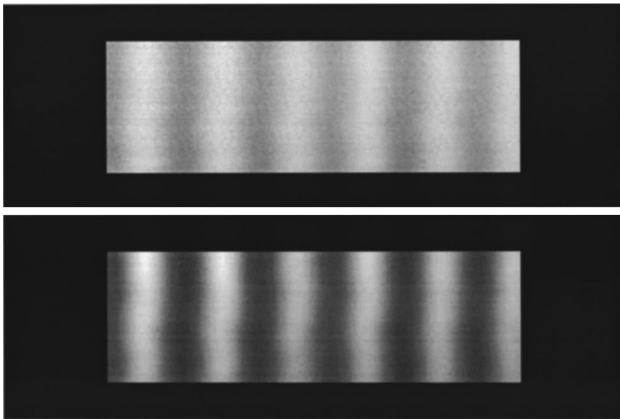


Fig. 12. Experimental images of the set of parallel bars of Fig. 11 obtained with our superresolving microscope. Upper image shows pixel intensities in type 1 mode. Lower image is the in-band superresolved image.

The microscope is an object-scanning device, so a three-dimensional piezo scanning stage shifts the object. The optical axis of the system remains stationary. Interactive software running on a personal computer controls the movements of the scanning stage through a digital-analog board while reading out the two detector single-photon counting outputs simultaneously. The software also renders the final image as the calibrated difference of the two measured signals.

The theoretical performance expected from the superresolving mask system is shown in Fig. 11 against that of a type 1 microscope. Figure 12 shows the experimental results. In these two figures the upper image shows a type 1 scan and the lower image is the scan in the superresolving mode. The focal-spot light power was 20 μ W, the sample time per pixel was 6 ms, and the images are 200×64 pixels.

For the calculation of Fig. 11 a function $f(\rho, z = 0)$, consisting of equal width parallel bars and spaces with a 250-nm period, was used, and its angular average $f_0(\rho, z = 0)$ was derived for any scanning position [see Eq. (3.1)]. Then the angular-averaged image $g_0(\rho)$ could be computed by sampling $f_0(\rho)$ and applying the operator

$A_{n,m;l}$ to it [Eq. (3.2)]. Here $g_0(\rho)$ is the blurred image at a specific scanning position. Thus Eq. (2.13) gives the reconstructed superresolved pixel value for this position. A mask function has been chosen that represents our mask in the experiment with seven singular functions. In case of the type 1 image, the pixel intensity arises from the same process when the mask function is set to unity for all ρ in Eq. (2.13).

No noise is present in either the theoretical or the experimental results shown in Fig. 12; the experimental data has been bandlimited to the seven singular functions used in the makeup of the mask by projecting the image onto them (off-line), thus removing the out-of-band photon and dark current noise. The modulation between bars, i.e., the calculated ratios of low intensity in the spaces to the high intensity in the bars, are 0.83 and 0.44 for the type 1 and superresolving microscopes, respectively. The experimental results give modulations of 0.80 for the type 1 and 0.43 for the superresolving microscope. For the present values of wavelength and NA, a period of 250 nm approximately represents the Rayleigh limit. The new microscope will thus Rayleigh resolve 70-nm-wide bars. As in our previous work at low aperture, these first controlled experimental images at high working aperture clearly show close agreement with the full superresolving gain in microscopy that we have predicted theoretically.

8. CONCLUSION

In this paper we have presented a full singular-value-decomposition analysis of the imaging of the high-NA fluorescence microscope giving both the spectrum and the singular functions and expanding significantly on the work of Ref. 5. Then, with these results, a new optical mask performing the analog implementation of an SVD-based, data-inversion algorithm has been designed. Following this, a numerical simulation of the performance of a microscope that uses our mask has been carried out and the resolution gains have been calculated. These results amply demonstrate that microscopes with binary masks can be superresolving in the lateral direction while preserving the good axial characteristics of the confocal microscope. Finally, initial experiments on a standard sample have been performed, and the predicted lateral performance improvement has been confirmed. Further experimental work is in progress and will be described in a later paper.

ACKNOWLEDGMENTS

This work was supported by grants from the Science and Engineering Research Council (grant GR/K 19150) and from the U.S. Army (grant DAAH04-95-1-0280). We are grateful to Bio-Rad Ltd. for continuing support throughout this project.

*I. Akduman's permanent address is the Faculty of Electrical and Electronics Engineering, Technical University of Istanbul, 80626, Istanbul, Turkey.

REFERENCES

1. J. G. Walker, E. R. Pike, R. E. Davies, M. R. Young, G. J. Brakenhoff, and M. Bertero, "Superresolving scanning optical microscopy using holographic optical processing," *J. Opt. Soc. Am. A* **10**, 59–64 (1993).
2. M. Bertero, P. Boccacci, R. E. Davies, F. Malfanti, E. R. Pike, and J. G. Walker, "Superresolution in confocal scanning microscopy: IV. Theory of data inversion by the use of optical masks," *Inverse Probl.* **8**, 1–23 (1992).
3. M. R. Young, S. H. Jiang, R. E. Davies, J. G. Walker, E. R. Pike, and M. Bertero, "Experimental confirmation of superresolution in coherent confocal scanning microscopy using optical masks," *J. Microsc.* **165**, 131–138 (1992).
4. J. Grochmalicki, E. R. Pike, and J. G. Walker, "Experimental confirmation of superresolution in incoherent scanning microscopy," *Pure Appl. Opt.* **2**, 565–568 (1993).
5. M. Bertero, P. Boccacci, G. J. Brakenhoff, F. Malfanti, and H. T. M. van der Voort, "Three-dimensional image restoration and superresolution in fluorescence confocal microscopy," *J. Microsc.* **157**, 3–20 (1990).
6. M. Bertero, P. Boccacci, F. Malfanti, and E. R. Pike, "Superresolution in confocal scanning microscopy: V. Axial superresolution in the incoherent case," *Inverse Probl.* **10**, 1059–1077 (1994).
7. V. S. Ignatowsky, "Diffraction by an objective lens with arbitrary aperture," *Trans. Opt. Inst. Petrograd* **1**(4), 1–36 (1921) (in Russian).
8. B. Richards and E. Wolf, "Electromagnetic diffraction in optical systems: II. Structure of the image field in aplanatic systems," *Proc. R. Soc. London, Ser. A* **253**, 358–379 (1959).
9. M. Bertero, P. Boccacci, M. Defrise, C. De Mol, and E. R. Pike, "Superresolution in confocal scanning microscopy: II. The incoherent case," *Inverse Probl.* **5**, 441–461 (1989).
10. M. Bertero and P. Boccacci, "Computation of the singular system for a class of integral operators related to data inversion in confocal microscopy," *Inverse Probl.* **5**, 935–957 (1989).
11. A. Papoulis, "Hankel transforms," in *Systems and Transforms with Applications in Optics* (McGraw-Hill, New York, 1968).
12. H. E. Fettes, "Lommel-type integrals involving three Bessel functions," *J. Math. Phys. (Paris)* **36**, 88–95 (1957).
13. J. Grochmalicki, E. R. Pike, J. G. Walker, M. Bertero, P. Boccacci, and R. E. Davies, "Superresolving masks for incoherent scanning microscopy," *J. Opt. Soc. Am. A* **10**, 1074–1077 (1993).
14. T. Wilson and C. Sheppard, *Theory and Practice of Scanning Optical Microscopy* (Academic, London, 1984).
15. A. E. Siegman, "Quasi-fast Hankel transform," *Opt. Lett.* **1**, 13–15 (1977).